JOURNAL OF Materials CHEMISTRY

Oxide ion conduction in A-site deficient La-Ti-Al-O perovskite

Hideki Yoshioka[a] **and Shinichi Kikkawa**[b]

[a]*Hyogo Prefectural Institute of Industrial Research, Suma, Kobe 654–0037, Japan*

[b]*The Institute of Scientific and Industrial Research, Osaka University, Ibaraki, Osaka 567–0047, Japan*

Oxide ion conduction in A-site deficient La–Ti–Al–O perovskites is demonstrated by complex impedance analysis and EMF measurements with an oxygen concentration cell. The oxide ion conductivity increases with decreasing the Al content. The enhancement of the conductivity has strong relation to the cation vacancy ordering and *c*-axis parameter expansion which were revealed by Rietveld refinement on the X-ray diffraction patterns. Dielectric relaxation which is remarkable considering the small Al content is explained by high ionic conductivity in the bulk grain and a high capacitance value in the grain boundary.

A number of titanates with perovskite structure have been developed for advanced dielectric materials such as $BaTiO_3$, $PbTiO_3$ and PLZT (Pb–La–Zr–Ti–O). Lanthanum titanate, $La_{2/3}TiO_3$, is expected to have a unique deficient perovskite-type structure with one-third of lanthanum sites (A-sites) vacant[1] and, therefore, to show unique electrical properties. However, pure $La_{2/3}TiO_3$ has not yet been prepared.[2]

The perovskite structure has been stabilized by changing its chemical composition slightly. Abe and Uchino prepared $La_{2/3}TiO_{3-\delta}$ perovskites with oxygen vacancy, δ, ranging from 0.007 to 0.079 under reduced oxygen pressures and examined the crystallographic properties.[3] They reported that the compound is orthorhombic and has a superstructure with a doubled unit cell along the *c*-axis when δ is small. They also claimed that ordering of the cation vacancies on the A-sites is responsible for the superstructure; namely, the LaO(1) plane contains a small amount of cation vacancies and the LaO(2) plane contains a large amount of cation vacancies which are alternately sited along the *c*-axis.

In the system $La_{2/3}TiO_3$-$SrTiO_3$, perovskite solid solutions were formed up to a composition of 94 mol% $La_{2/3}TiO_3$; moreover, the superstructure was observed at compositions containing more than 70 mol% of $La_{2/3}TiO_3$.[4] Dielectric relaxation was observed for the system $La_{2/3}TiO_3$-$SrTiO_3$, but no detailed information was given.[5] As Sr^{2+} enters the A-site of the perovskite structure, the amount of A-site vacancies is reduced from 1/3 to $1/3-x/3$ as shown in eqn. (1), leading to the stabilization of the perovskite structure.

$$(1-x)\ La_{2/3}TiO_3 + x\ SrTiO_3 \rightarrow (La_{2/3-2x/3}Sr_x)TiO_3 \quad (1)$$

Alkali metals such as Na and Li also stabilize the perovskite structure.[6] The amount of A-site vacancies is reduced by filling them up with Na or Li. The compounds thus obtained are known to be good alkali metal ion conductors.[7]

Recently, Negas *et al.*,[8] Škapin *et al.*[9] and Yoshioka[10] found that the perovskite structure was also stabilized by partial substitution for Ti^{4+} with Al^{3+}. In this system the A-site vacancies decreases from 1/3 to $1/3-x/3$ by B-site substitution as shown in eqn. (2).

$$(1-x)\ La_{2/3}TiO_3 + x\ LaAlO_3 \rightarrow La_{2/3+x/3}(Ti_{1-x}Al_x)O_3 \quad (2)$$

A remarkable dielectric relaxation was observed for the La–Ti–Al–O perovskites when the Al content was small ($x=$ 0.05–0.15).[10] The dielectric relaxation was characterised by a maximum in dielectric loss and an increase in dielectric constant (relative permittivity) at low frequency; there, as yet, is no explanation for this phenomenon.

In the present study, systematic investigations of the dielectric and complex impedance measurements were made on La–Ti–Al–O perovskites. This work demonstrates oxide ion conduction in the La–Ti–Al–O perovskites which is responsible for the dielectric relaxation. The oxide ion conduction in the A-site deficient perovskites is discussed in relation to the structural information obtained by the Rietveld analysis for the powder X-ray diffraction patterns.

Experimental

Sample preparation and characterisation

All samples were prepared by solid state reactions of La_2O_3, TiO_2 and Al_2O_3 powders of purity >99.9%. Compositions tested are shown in Table 1; samples with x ranging from 0 to 0.2 for $(1-x)La_{2/3}TiO_3$–$xLaAlO_3$ were prepared. Starting powders were prefired at 1273 K for 4 h, weighed, and well ground with ethanol in an agate mortar.

The mixtures were calcined at 1623 or 1673 K for 8 h in a flowing N_2–O_2 atmosphere and reground. Calcination and regrinding were repeated 4–8 times until no change in the powder X-ray diffraction patterns was observed. The calcined powders were pressed into pellets and sintered at 1623 or 1673 K for 8 h in a flowing O_2 atmosphere.

Phases in the samples were identified by X-ray powder diffraction analysis. Sintered densities were measured with immersion in water by the Archimedes method. A scanning electron microscope was used to observe the microstructures and measure the grain sizes.

Pellets of ZrO_2 stabilized with 15 mol% CaO (CSZ) were also prepared by a standard powder method. They were used to check the performance of electrical measurements.

Complex impedance and dielectric measurements

Prior to the measurements, both sides of the sample pellets were polished and, if needed, heat-treated in an atmosphere of O_2, Ar or air. After this, Pt–Pd electrodes were formed on

Table 1 Nominal compositions of the samples

sample	x	$La_{2/3}TiO_3$	$LaAlO_3$	nominal composition
LT	0	1.0	0	$La_{0.6667}TiO_3$
LTA05	0.05	0.95	0.05	$La_{0.6833}Ti_{0.95}Al_{0.05}O_3$
LTA10	0.10	0.90	0.10	$La_{0.7000}Ti_{0.90}Al_{0.10}O_3$
LTA15	0.15	0.85	0.15	$La_{0.7167}Ti_{0.85}Al_{0.15}O_3$
LTA20	0.20	0.80	0.20	$La_{0.7333}Ti_{0.80}Al_{0.20}O_3$

both sides by sputtering. Dielectric constant, dielectric loss, absolute value of vector impedance, and phase angle were measured simultaneously by the two-terminal method using YHP 4274A and 4275A LCR meters with an applied voltage of 1 or 5 V, frequency range from 100 to 4 MHz, and temperature range from 293 to 1073 K. The results were reproducible for the heating cycles indicating that the oxidation state did not change. Thus, in general, we employed the same atmospheric conditions for measurements as that for the sintering or annealing.

EMF measurements with a gas concentration cell

The open circuit voltage on the sintered pellets with sputter-deposited electrodes was measured using a Keithley 617 digital meter in a gas concentration cell at 773–873 K. Oxygen partial pressures ranging from 0.1 to 0.9 were used for one side; atmospheric pressure was employed for the other side as a reference gas. Ionic transport number was calculated from the slope in the plot of the measured open circuit voltage *vs.* the oxygen partial pressure which was compared with the theoretical value of the Nernst equation.

Rietveld analysis

Powder X-ray diffraction patterns for the Rietveld analysis were obtained by a step scanning method with a scanning interval of 0.04° using a rotating-anode type X-ray generator. The Rietveld analysis software, RIETAN, written by Izumi [11] was used to refine the precise structural parameters.

Results and Discussion

Complex impedance analysis

All sintered pellets were brownish white and their sintered densities were 95–98% of theoretical. Microscopic observation by scanning electron microscopy revealed considerable grain growth; the average grain sizes were 5–15 μm. X-Ray diffraction patterns in the composition range $x=0.05$–0.20 showed the presence of perovskite having a superstructure with a doubled *c*-axis parameter. Our phase identification was in good agreement with that reported by Škapin *et al.*[9] A trace of an impurity $La_2Ti_2O_7$ pyrochlore phase existed and its amount slightly increased in LTA20. It is noteworthy that the partial substitution stabilized the perovskite structure. In pure $La_{2/3}TiO_3$ composition (LT), no perovskite phase formed and a mixture of $La_2Ti_2O_7$ and $La_4Ti_9O_{24}$ was obtained.

Complex impedance results measured on LTA05 and LTA20 at 873 K are shown in Fig. 1. Two semicircles were observed in the Cole–Cole plots for both LTA05 and LTA20. Frequencies at maximum Z'' (the top of semicircles) and minimum Z'' (the neck between semicircles) are also shown. Note that the maximum of the low frequency semicircle for LTA05 was lower than the frequency we could measure with our LCR meter (100 Hz); for this reason, the maximum frequency was estimated by extrapolation. The higher frequency semicircle of LTA05 is very small compared with the lower frequency semicircle. In LTA20, two semicircles are similar in size; moreover, considerable overlap of two semicircles is observed.

It is known that two semicircles in an impedance plot are well explained by an equivalent circuit shown in Fig. 2. If we assume that R_1C_1 is less than R_2C_2, the parallel circuit consisting of R_1 and C_1 corresponds to the higher frequency semicircle; the R_2 and C_2 circuit corresponds to the lower frequency semicircle. These semicircles are well separated when the time constants, τ_1 ($=R_1C_1$) and τ_2 ($=R_2C_2$), differ greatly; the two semicircles are considerably overlapped when the time constants are of a similar magnitude. Table 2 lists the values of τ_1, τ_2, R_1, R_2, C_1 and C_2 obtained from the frequencies and impedance at the top of the semicircles.

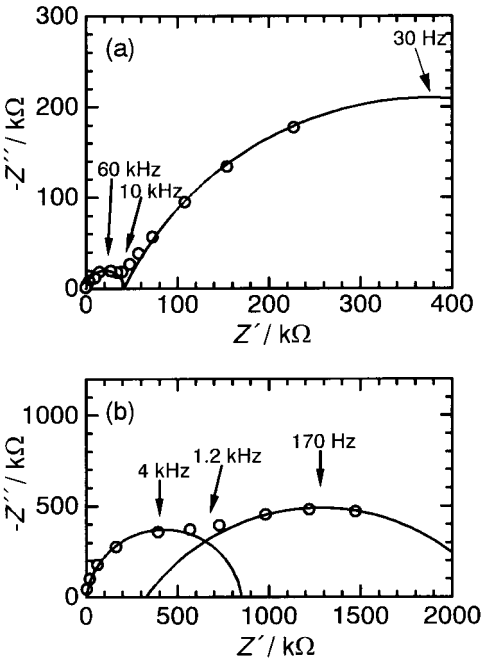

Fig. 1 Impedance plots of (a) LTA05 and (b) LTA20 measured at 873 K

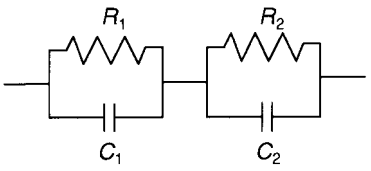

Fig. 2 Equivalent circuit used for LTA05 and LTA20

Table 2 Time constants and resistance and capacitance values of LTA05 and LTA20. These parameters were calculated from the data plotted in Fig. 1(a) and (b), assuming a parallel equivalent circuit as shown in Fig. 2

sample	T/K	τ_1/ms	τ_2/ms	R_1/kΩ	R_2/kΩ	C_1/pF	C_2/nF
LTA05	873	0.017	33	42	740	400	45
LTA20	873	0.25	5.9	850	2340	310	2.5

As can be seen from Table 2, R_1 of LTA05 is remarkably small, about 1/20 of that of LTA20. Also, C_2 of LTA05 is about 20 times larger than that of LTA20. Consequently, the time constants τ_1 and τ_2 of LTA05 differ by more than 3 orders of magnitude, resulting in a clear separation of the semicircles. In contrast, the time constants of LTA20 differ by only 20 causing a large overlap of the semicircles.

Effects of sample thickness and measuring atmosphere on the impedance

Impedance plots for ceramic samples often give multiple semicircles as observed in Fig. 1. These semicircles are often referred to polarization in bulk grains, grain boundaries, and electrode interfaces in order of decreasing frequency. It is also known that the semicircle arising from grain boundaries or electrode interfaces is sometimes missing. Therefore, impedance measurements were performed with changing sample thickness in order to investigate what is responsible for each semicircle in the impedance plot of LTA shown in Fig. 1.

Fig. 3 shows the impedance plots at 773 K for two LTA05 samples having different thickness; the thicker sample has approximately double the thickness and the same electrode area as the thinner one. The higher frequency semicircle of the thicker sample is doubled in size, suggesting that the polariz-

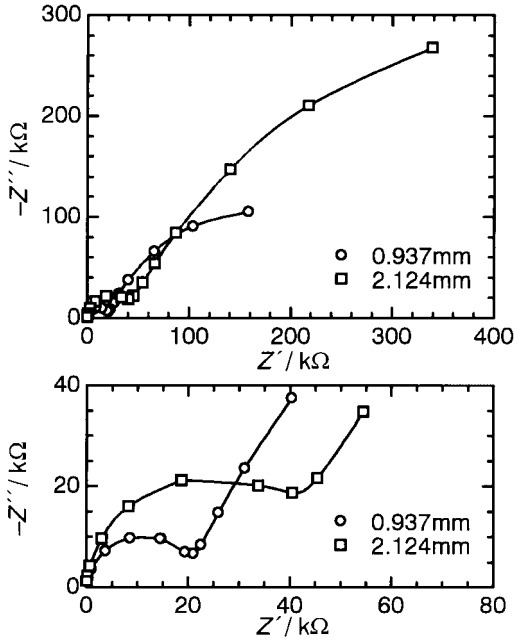

Fig. 3 Impedance plots for two LTA05 samples having different thicknesses of 0.937 mm (○) and 2.124 mm (□) measured at 773 K

ation occurs in the bulk grains. Also, the size of the lower frequency semicircle changes in accordance with the sample thickness. This indicates that the lower frequency semicircles arise from polarization in the grain boundaries, since the semicircle due to the electrode interface polarization would not change with the sample thickness.

The effect of measuring atmosphere on the impedance was next evaluated to explore the conduction mechanisms in the bulk grains and the grain boundaries. Fig. 4 shows a comparison of the measured results for LTA05 in flowing O_2 or Ar after sintering in O_2. The bulk resistance of 19 kΩ is almost the same for both samples. In contrast, the grain boundary resistance of 260 kΩ in O_2 is 1.5 times larger than the value in Ar (170 kΩ).

The decrease in the grain boundary resistance in flowing Ar reveals the electronic conductive nature of the grain boundaries. Reduction in flowing Ar enhanced *n*-type conduction in the grain boundaries. By contrast, the bulk resistance showed little change, suggesting that the dominant ionic conduction occurs in the bulk grains at 833 K.

Temperature dependence of conductivity

The temperature dependence of bulk and grain boundary conductivity was investigated in (*i*) O_2, (*ii*) air and (*iii*) Ar. Samples measured were (*i*) LTA05 sintered in O_2, (*ii*) LTA05 annealed in air for 1 h at 1273 K after sintering and (*iii*) LTA05

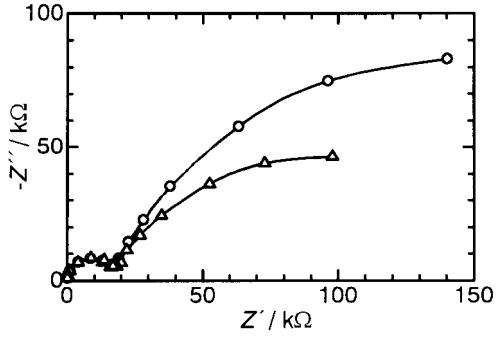

Fig. 4 Impedance plots of LTA05 measured in O_2 (○) and Ar (△) at 833 K after sintering in O_2

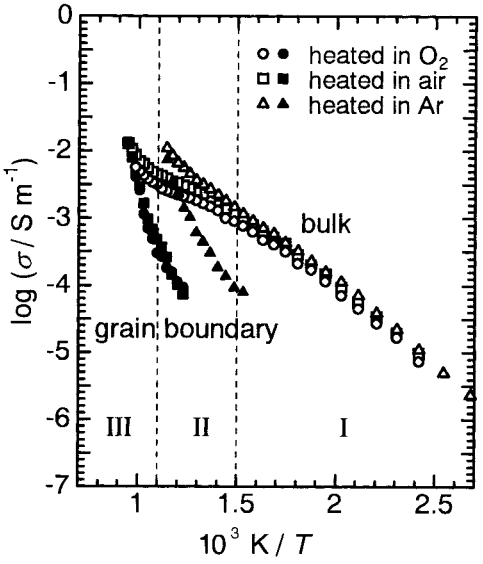

Fig. 5 Temperature dependence of bulk and grain boundary conductivities for LTA05 heated in various atmospheres: heated in O_2 (○, ●), air (□, ■) and Ar (△, ▲) for bulk (open symbols) and grain boundary (filled symbols)

annealed in Ar for 1 h at 1273 K after sintering, respectively. The results on bulk and grain boundary conductivities are shown in Fig. 5. The bulk conductivity for the sintered sample [(*i*), open circles] can be divided into three regions. In region I, where the temperature is <673 K (*i.e.* $1000/T<1.5$), the bulk conductivity increases linearly with temperature and the activation energy was calculated as 40 kJ mol^{-1} (0.4 eV). Region II extends from 673 to 873 K ($1.5<1000/T<1.1$) with an activation energy of 30 kJ mol^{-1} (0.3 eV). In regions I and II, ionic conduction is believed to be dominant in the bulk grains, as discussed in the previous section. The observed low activation energies also suggest the dominant contribution of ionic conduction. The activation energy increases again in region III above 873 K.

Bulk conductivity in air [(*ii*), open squares] shows a similar temperature variation with slightly larger values than in O_2. Also, the grain boundary conductivity is similar for measurements in air and in O_2. As a whole, the electrical properties of LTA05 are very similar in air and in O_2; both bulk and grain boundary conductivities were enhanced with sample reduction in air at high temperature similarly as in O_2.

The Ar-annealed sample [(*iii*), open triangles] shows a basically identical bulk conductivity with those annealed in air and O_2 in region I below 673 K. However, it differs in terms of the temperature dependence above 673 K; the activation energy continuously increases in region II with no intermediate reduced activation energy. It is also noticed that the grain boundary conductivity (filled triangles) starts to increase at much lower temperature than for samples in air and in O_2. This reveals that the bulk conduction in an Ar-annealed sample is ionic below 673 K, while an electronic contribution may be present both in the bulk and grain boundary conduction above 673 K. Reduction proceeds into the bulk grain upon high temperature annealing in Ar.

Fig. 6 shows the temperature variations of bulk conductivity of LTA sintered in O_2 with various compositions. LTA05 has the highest conductivity below 873 K. The bulk conductivity decreases with increasing the Al content to LTA10 and LTA15. LTA20 has one tenth the conductivity of LTA15. The conductivities are similar among these samples above 873 K where the electronic contribution is dominant.

EMF measurement and ionic conduction species

Ionic conduction is assumed to be dominant below 873 K in the samples heated in air or in O_2 in the above discussion.

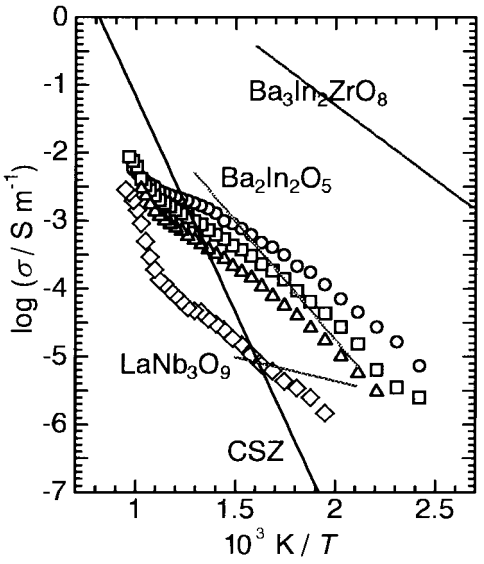

Fig. 6 Temperature dependence of bulk conductivity of LTA with various compositions sintered in O_2: LTA05 (○), LTA10 (□), LTA15 (△) and LTA20 (◇). Oxide ion conductivities of various compounds are also shown for comparison.

EMF measurements were performed on LTA05 using an oxygen gas concentration cell to evaluate ionic transport number, *t*. Open circuit voltage was measured in the concentration cell against air as a reference electrode. It continuously changed with oxygen concentration in an N_2–O_2 mixture on the measuring electrode. This phenomenon supports that bulk ionic conduction occurs in LTA05. Table 3 lists ionic transport numbers at various temperatures. At 773 K this is very close to unity showing almost pure ionic conduction; above this temperature an increased electronic contribution reduced the ionic transport number.

The appearance of an open circuit voltage does not necessarily mean that the mobile species is oxide ion. Nevertheless, it is reasonable to consider oxide ion conduction since ionic conduction of tri- or tetra-valent cations has not been so far satisfactorily demonstrated except for the trivalent cation conductors, $Al_2(WO_4)_3$[12] and $Sc_2(WO_4)_3$.[13] Direct experimental determination of oxide ion conduction using the oxygen gas pumping method, however, could not be applied to LTA because of increasing electronic conduction at high temperature and insufficient ionic conductivity for the low temperature operation.

To confirm oxide ion conduction, we investigated a change in the terminal voltage by connecting an external resistance to the gas concentration cell. The terminal voltage decreased by two-thirds upon connecting a 10 MΩ resistance; however, a stable voltage was observed over 30 h. This results indicate that the electrical current could be drawn stably from the concentration cell and thus indicates dominant oxide ion conduction. The decrease in the terminal voltage is probably due to insufficient ionic conductivity and large grain boundary resistance.

It is noteworthy that the conductivity of LTA05 at 773 K did not vary from flowing air to flowing dry N_2. This indicates that the contribution of the proton conduction is small in LTA05, in contrast to proton conducting *p*-type perovskite oxides.

Table 3 Ionic transport number of LTA05

T/K	*t*
773	0.99
823	0.91
873	0.62

Dielectric relaxation

LTA05 showed remarkable dielectric relaxation as previously reported.[10] This is characterised by a maximum in dielectric loss *vs.* frequency and an increase in dielectric constant with decreasing frequency. With an increase in the Al content the maximum in dielectric loss showed a remarkable broadening . Finally, a maximum was no longer observed for LTA20; only a slight increase was observed at around 1 kHz.

Comparison of the dielectric and impedance measurements revealed that the frequencies at the neck in Fig. 1 directly correspond to the frequencies of the dielectric loss maxima. This correspondence can be understood from the following relation;

$$\tan \delta = 1/\tan \theta = |Z'|/|Z''|$$

where θ is the impedance phase angle. This equation means that the dielectric loss of LTA05 shows a pronounced maximum because $|Z''|$ is small enough at the neck. Because of the large overlap of the semicircles, $|Z''|$ of LTA20 is not so small at the neck, corresponding to the only slight increase in the dielectric loss.

As observed in Table 1, the clear separation of the semicircles on LTA05 is ascribed to the small R_1 (bulk grain resistance) and large C_2 (grain boundary capacitance). Moreover, at this temperature, bulk grain conductivity is dominated by oxide ion conduction. Thus it is concluded that the dielectric relaxation in LTA05 is attributed to the high oxide ion conductivity in the bulk grain and a high capacitance value in the grain boundary.

Rietveld analysis

X-Ray diffraction patterns of LTA showed superstructure diffraction lines of a doubled lattice parameter along the *c*-axis similarly to $La_{2/3}TiO_{3-\delta}$.[3] Rietveld refinement was started from a structure model shown in Fig. 7. Two types of LaO plane are alternately built up; LaO(1) and LaO(2) planes have a small and large amount of La vacancies, respectively. Ti^{4+} and Al^{3+} are randomly distributed on the B-sites. The space group was assumed to be orthorhombic *P*/*mmm* for LTA05 and LTA10 since there are 200, 020 and 002 diffraction peaks. LTA15 and LTA20 have tetragonal *P*4/*mmm* lattices. Isotropic thermal parameters were used for all constituent ions to converge the preliminary refinement. A common thermal parameter was applied to all oxide ions.

The crystal structure could be refined to reasonable values as shown in Table 4. Fig. 8 shows the variation of the lattice parameters and the cube root of the cell volume *vs.* Al content, *x*. LTA20 is very close to a cubic perovskite structure except

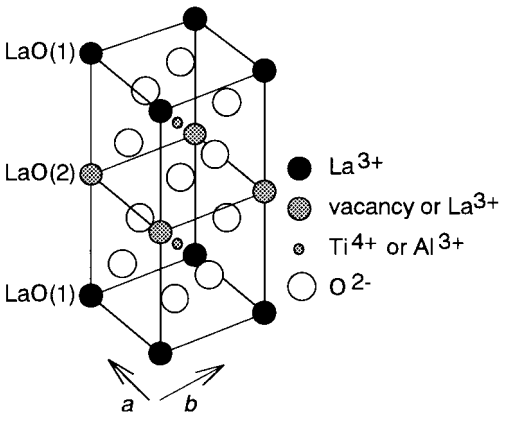

Fig. 7 Structure model of LTA perovskite used for the Rietveld analysis

Table 4 Experimental conditions and results of the Rietveld analysis on LTA

x		0.05	0.10	0.15	0.20
radiation		CuKα	CuKα	CuKα	CuKα
range 2θ/°		10–130	10–130	10–130	10–130
step width		0.04	0.04	0.04	0.04
crystal system		orthorhombic	orthorhombic	tetragonal	tetragonal
space group		*P*/*mmm*	*P*/*mmm*	*P*4/*mmm*	*P*4/*mmm*
reliance factor	R_{wp} (%)	16.78	15.31	17.96	18.38
	R_p (%)	12.29	11.16	13.68	13.98
	R_I (%)	6.10	5.26	7.78	9.05
	R_f (%)	3.85	3.57	5.26	6.84
lattice parameter	a/nm	0.38589(1)	0.38587(1)	0.38625(1)	0.38612(4)
	b/nm	0.38704(1)	0.38673(1)	0.38625	0.38612
	c/nm	0.77754(2)	0.77581(2)	0.77372(3)	0.77228(15)
occupation factor	La(1)	0.969(7)	0.966(6)	0.943(10)	0.867(12)
	La(2)	0.398	0.434	0.490	0.600
position, z	Ti,Al	0.262(1)	0.261(1)	0.259(3)	0.258(4)
	O(1)	0.242(8)	0.241(10)	0.236(4)	0.241(6)
	O(2)	0.240(9)	0.231(10)	0.236	0.241
thermal parameter,	La(1)	0.44(10)	0.45(9)	0.35(15)	0.26(25)
$B/10^{-2}$nm^2	La(2)	0.54(22)	0.38(18)	0.09(27)	0.16(33)
	Ti,Al	0.43(14)	0.44(13)	0.37(20)	0.17(24)
	O	2.09(40)	1.44(29)	0.87(41)	1.16(49)

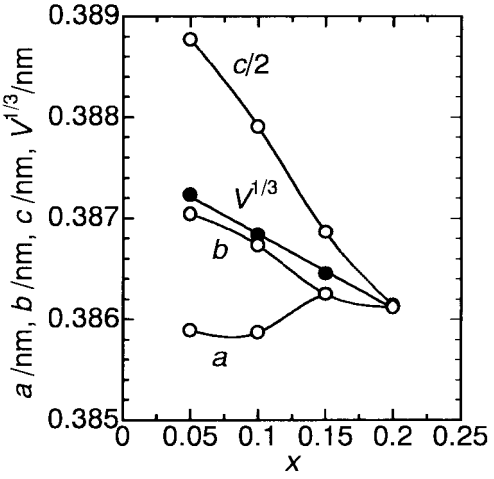

Fig. 8 Lattice parameters *versus* composition of LTA

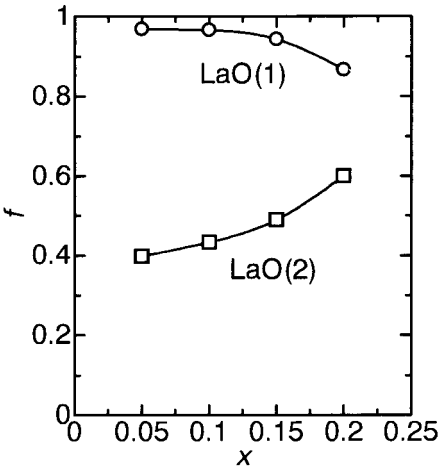

Fig. 9 La^{3+} occupation factors in LaO(1) and LaO(2) planes *versus* composition of LTA

for the existence of cation vacancy ordering. The cell volume of LTA increases linearly with decreasing x. The expansion of 0.3% from LTA20 to LTA05 is mainly due to the difference in the ionic radii between Ti^{4+} (0.0605 nm) and Al^{3+}(0.0530 nm).[14] A marked increase in the c-axis parameter with decreasing x, however, is noted; the lattice expansion along the c-axis is 0.7%. The c-axis expansion is closely related to the cation vacancy ordering discussed below. The occupation factors of La in the LaO planes are shown in Fig. 9. It reveals that almost all A-site vacancies of LTA05 and LTA10 are distributed in the LaO(2) plane. A decrease in the LaO(1) occupation factor together with an increase in LaO(2) make LTA20 close to an ordinary cubic perovskite structure, as is also seen from the lattice parameter variation in Fig. 8.

The ionic displacements of LTA05 are shown in Fig. 10. As a result of the cation vacancy ordering, the LaO(1) plane has a positive charge and LaO(2) has a negative charge. The B-site ions of Ti^{4+} and Al^{3+} approach the LaO(2) plane to 9 pm because of an attractive force to the LaO(2) plane. Oxide ions O(1) and O(2) in the $(Ti,Al)O_2$ plane lie 8 pm apart due to a repulsive force from the LaO(2) plane and by direct oxide ion contact. The (Ti, Al)O_6 octahedron is considerably distorted.

Unexpectedly large thermal parameters were observed on oxide ions in LTA05. This suggests that the conducting ionic species is oxide ion. Thermal parameters decreased with x as shown in Fig. 11 in decreasing order with ionic conductivity.

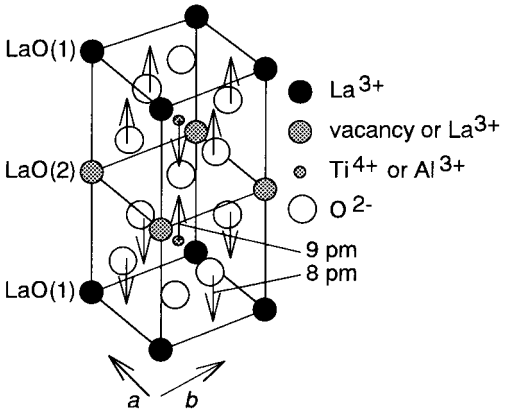

Fig. 10 Ionic displacements in LTA refined by the Rietveld analysis

Oxide ion conductivity in the A-site deficient perovskite oxide

Bulk conductivity of LTA with various compositions along with ionic conductivity of the related compounds are shown

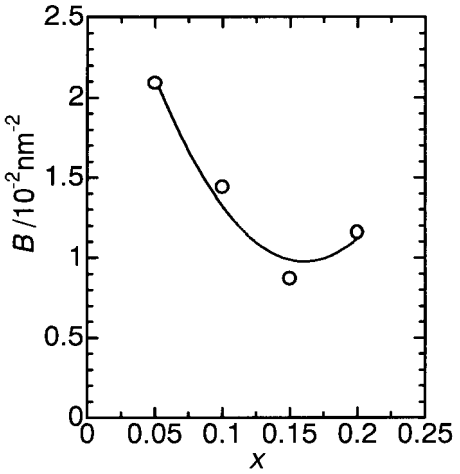

Fig. 11 Oxide ion thermal parameter *versus* composition of LTA

in Fig. 6. Zirconium oxide stabilized by CaO (CSZ) is a typical oxide ion conducting ceramic which shows high ionic conductivity at high temperatures. Owing to the large activation energy (0.8–1.0 eV), however, its ionic conductivity is lower than that of LTA05 below 800 K.

Few perovskite oxides have high oxide ion conductivity; Goodenough *et al.* prepared a series of Ba–In–O perovskites with relatively high oxide ion conductivity at low temperature.[15] Barium indium oxide ($Ba_2In_2O_5$) has 1/6 oxide ion vacancies arranged in an ordered manner. The activation energy of 0.74 eV is somewhat larger than of LTA05; the conductivity at 700 K is comparable to LTA05. Disordered oxide ion vacancies in $Ba_3In_2ZrO_8$ lead to much higher oxide ion conductivity as shown in Fig. 6; the activation energy is also lowered to 0.6 eV which is identical to that of LTA05. The disadvantage of these Ba–In–O perovskites is *p*-type electronic conduction in air with the ionic transport number being 0.93–0.96 at 773 K.

Lanthanum niobate ($LaNb_3O_9$) is a perovskite oxide with a large number of A-site vacancies. It has been reported to be a La ion conductor with fairly low conductivity and an extremely small activation energy of 0.19 eV.[16] The structure of $LaNb_3O_9$ resembles that of LTA05 having a superstructure with a doubled unit cell along the *c*-axis with 2/3 of the La site vacant. Oxide ions may also contribute to the conduction in $LaNb_3O_9$.

As distinct from other oxide ion conductors, the ionic conduction in LTA has unique characteristics. (*i*) LTA shows high ionic conductivity when the Al content is small. An increase in the cell volume with decreasing Al content may contribute to the enhancement of the ionic conductivity, but the cell volume increases by at most 0.3% from LTA20 to LTA05. The effect of the composition on the ionic conductivity is thus not explained by the cell volume only. Both the amount of A-site vacancies and the degree of order in the vacancy distribution increases with decreasing Al content. Therefore, the high ionic conductivity is strongly related to the increase in the amount of cation vacancies in the LaO(2) plane. Moreover, oxide ions in upper and lower sides are distant from the LaO(2) plane, resulting in a low density in the vicinity of the LaO(2) plane. This structure probably favors ionic condition.

(*ii*) The activation energy is small. The activation energy of LTA05 is very small compared to other typical oxide ion conductors; the value is comparable with or somewhat lower than those of Ba–In–O perovskites which have 1/6 vacant oxide ion sites. An activation energy of ionic conduction consists of two contributions: (*a*) the energy of jumping barriers existing in the bottleneck of the conduction pass, and (*b*) the energy of creating vacancies in the neighboring site of the jumping ions. The activation energy of Ba–In–O perovskites is equal to the energy of jumping barriers, since the compounds contain many oxide vacancies. Since LTA05 has a similar activation energy, it is assumed that there are many ionic jump sites for oxide ions in LTA05.

We thank N. Imanaka, H. Sakaguchi and I. Matsubara for helpful discussions.

References

1 M. Kestigian and R. Ward, *J. Am. Chem. Soc*., 1954, **76**, 6027.
2 J. B. MacChesney and H. A. Sauer, *J. Am. Ceram. Soc*., 1962, **45**, 416.
3 M. Abe and K. Uchino, *Mater. Res. Bull*., 1974, **9**, 147.
4 T. Y. Tien and F. A. Hummel, *Trans. Br. Ceram Soc*., 1967, **66**, 233.
5 J. Kainz, *Ber. Deutsch. Keram. Ges*., 1958, **35**, 69.
6 A. G. Belous, G. N. Novitskaya, S. V. Polyanetsukaya and Yu. I. Gornikov, *Izv. Akad. Nauk SSSR, Neorg. Mater*., 1987, **12**, 470.
7 Y. Inaguma, C. Liquan, M. Itoh, T. Nakamura, T. Uchida, H. Ikuta and M. Wakihara, *Solid State Commun*., 1993, **86**, 689.
8 T. Negas, G. Yeager, S. Bell and R. Amren, *NIST Spec. Publ*., 1991, **804**, 21.
9 S. Škapin, D. Kolar and D. Suvorov, *J. Am. Ceram. Soc*., 1993, **76**, 2359.
10 H. Yoshioka, *Jpn. J. Appl. Phys*., 1994, **33**, L945.
11 F. Izumi, *Nippon Kessyou Gakkaishi*, 1985, **27**, 23.
12 Y. Kobayashi, T. Egawa, S. Tamura, N. Imanaka and G. Adachi, *Chem. Mater*., 1997, **9**, 1649.
13 N. Imanaka, Y. Kobayashi and G. Adachi, *Chem. Lett*., 1995, 433.
14 R. D. Shannon and C. T. Prewiitt, *Acta Crystallogr., Sect. B*, 1969, **25**, 925.
15 J. B. Goodenough, J. E. Ruiz-Diaz and Y. S. Zhen, *Solid State Ionics*, 1990, **44**, 21.
16 A. M. George and A. N. Virkar, *J. Phys. Chem. Solids*, 1988, **49**, 743.

Paper 8/01926F; *Received* 9*th March*, 1998